Multi-Resolution Dynamic Mode Decomposition for Wideband Harmonic Instability Identification

Kong, Rui; Sahoo, Subham; Song, Yubo; Xiao, Yi; Gao, Chao; Blaabjerg, Frede

Published in:
IEEE Transactions on Power Electronics

DOI (link to publication from Publisher):
10.1109/TPEL.2024.3519978

Publication date:
2024

Document Version
Accepted author manuscript, peer reviewed version

Multi-Resolution Dynamic Mode Decomposition for Wideband Harmonic Instability Identification

Kong, Rui; Sahoo, Subham; Song, Yubo; Xiao, Yi; Gao, Chao; Blaabjerg, Frede

Published in:
I E E E Transactions on Power Electronics

DOI (link to publication from Publisher):
10.1109/TPEL.2024.3519978

Publication date:
2024

Document Version
Accepted author manuscript, peer reviewed version

Multi-Resolution Dynamic Mode Decomposition for Wideband Harmonic Instability Identification

Rui Kong, *Student Member, IEEE,* Subham Sahoo, *Senior Member, IEEE,* Yubo Song, *Member, IEEE,* Yi Xiao, *Student Member, IEEE,* Chao Gao, and Frede Blaabjerg, *Fellow, IEEE*

***Abstract*—Mode identification of harmonic instability in modern power electronics-dominated power grids facilitates oscillation detection, stability assessment and further damping control. However, complex oscillation components and possible uncharacteristic transient variations of the signal pose challenges to robust and accurate mode identification of oscillation signals. In this paper, an identification method based on multi-resolution dynamic mode decomposition (MR-DMD) algorithm is leveraged to extract dominant system modes with time-frequency information at multiple frequency decomposition levels and temporal subsets, thereby improving robustness in handling missing data. In addition, key algorithm parameters are defined and derived to reveal their impact on the algorithm's performance, while a framework of parameter design is further developed to optimize the identification results. The proposed method and framework are verified and interpreted under diverse oscillation scenarios using real measurement data from experimental conditions.**

***Index Terms*—Grid-tied converter, oscillation mode identification, dynamic mode decomposition, multi-resolution analysis, parameter design.**

I. Introduction

With the large-scale deployment of grid-tied converters for renewable energy sources [1], energy storage [2], electric high-speed railways [3], etc, the legacy power grids are evolving into modern power electronic converter-based power systems. Depending on specific control topologies and power system conditions, the small-signal dynamics of power electronic converters may bring negative damping to the system in different frequency ranges [4]. Thus, harmonic instability phenomena might be provoked from the low/sub-synchronous frequencies [3], [5] to high frequencies around multiple kHz [6], resulting in power quality degradation and even disruptions to the power supply, affecting the safe and reliable operation of the system.

To this end, oscillation mode identification for stability assessment is essential. There are some model-based approaches aiming at the detailed modeling of dynamic system characteristics, e.g. eigenvalue analysis with state-space models [7], which are limited by the modeling complexity and unknown system parameters. Impedance measurements are capable of assessing system stability with measured frequency responses, but the frequency-scan process is time-consuming, and additional harmonic source injection is required [8]. In comparison, data-driven identification techniques can be implemented only using sampled data, which is more practical for black-box cases. Based on the recorded signal data, mode identification techniques can extract oscillation characteristics as the verification basis for further stability modeling and analysis, while its online application can detect instability events and quantify oscillation risks [9]. The extraction of frequency and damping information at the early stage of oscillation for stability prediction can effectively avoid serious hazards by committing corresponding damping control measures for instability mitigation [10].

As a fundamental yet vital method for time series signal analysis, discrete Fourier transform (DFT) [11] focuses on spectral characteristic analysis of stationary signals. On this basis, some improved algorithms such as fast Fourier transform (FFT) [12] and recursive DFT [13] are employed for real-time harmonic detection in active power filters (APF). The categorization and comparison of classical real-time harmonics extraction and control techniques are given in Table I, covering instantaneous reactive power theory (IRPT) and its variants [14]–[16], synchronous dq-frame (SDQF) methods [17], modulation-function integral observer (MFIO) [18], etc. However, these methods are dedicated to harmonic extraction but cannot capture critical damping properties for stability assessment. Thus, mode identification techniques that can extract eigenvalues are more appropriate to intuitively assess the system stability. Prony [19], matrix pencil (MP) [20], and eigensystem realization algorithm (ERA) [21] are reported and compared in [22] as three major identification methods for the power system. All of them find eigenvalues depending on Hankel matrices, but the system state matrix or state variables lack of clear physical significance. Dynamic mode decomposition (DMD) derived from Koopman theory [23] has recently been applied to oscillation and voltage flicker identification in power systems [9], [24], [25]. DMD can approximate the best-fit state matrix from the measured data snapshots with well-defined state variables to extract accurate DMD modes, while signal reconstruction and prediction can be performed based on the identified modes.

The mode identification should be robust considering the uncharacteristic transient variation of signals in practical applications, such as missing data due to hardware failures or cyber-attacks [26]. However, the aforementioned identification algorithm containing Prony, MP, ERA and DMD are single-resolution methods, which process all sampled data at one time to provide a full-rank approximation without time domain information, resulting in poor robustness to process transient time behaviors [27]. As shown in Fig. 1, the modes can be

Rui Kong, Subham Sahoo, Yubo Song & Frede Blaabjerg are with the Department of Energy, Aalborg University, 9220 Aalborg East, Denmark (e-mail: {ruko,sssa,yuboso,fbl}@energy.aau.dk). Yi Xiao is with the College of Electrical Engineering, Zhejiang University, Hangzhou 310013, China (e-mail: yi_xiao@zju.edu.cn). Chao Gao is with the Department of Electronic Engineering, the Chinese University of Hong Kong, Hong Kong, China (e-mail: chaogao@link.cuhk.edu.hk)

TABLE I
COMPARISON OF REAL-TIME HARMONIC DETECTION AND MODE IDENTIFICATION METHODS.

Category	Technique	Frequency information	Damping information	Harmonic extraction	Robustness of transient variation	Remarks
Real-time harmonic detection and control	DFT-related [11]–[13]	✓	×	✓	×	Spectral leakage and fence effect
	IRPT-related [14]–[16]	×	×	✓	—	Affected by filter performance in detection circuits
	SDQF [17]	×	×	✓	—	Phase-locked loop is required
	MFIO [18]	×	×	✓	—	More cost for selective harmonic compensation
Mode identification	Prony [19]	✓	✓	×	×	Undefined state matrix and state variables
	MP [20]	✓	✓	×	×	Undefined state matrix and state variables
	ERA [21]	✓	✓	×	×	Undefined state variables
	EMD [28]	×	×	✓	×	Uncontrolled decomposition process
	DMD [9], [24], [25]	✓	✓	×	×	Transient time behavior cannot be handled
Time-frequency analysis	WT [29]	✓	×	✓	✓	Difficulty in selecting wavelet basis functions
	MR-DMD [30]	✓	✓	✓	✓	Difficulty in setting parameter

✓: Yes, ×: No, —: Inapplicable, DFT: Discrete Fourier Transform, IRPT: Instantaneous Reactive Power Theory, SDQF: Synchronous dq-Frame, MFIO: Modulation-Function Integral Observe, MP: Matrix Pencil, ERA: Eigensystem Realization Algorithm, EMD: Empirical Mode Decomposition, DMD: Dynamic Mode Decomposition, WT: Wavelet Transform, MR-DMD: Multi-Resolution Dynamic Mode Decomposition

identified in the Laplacian domain as $s = \sigma + j\omega$, where $f = \omega/2\pi$ is the oscillation frequency, and σ indicates the signal decaying over time, namely mode damping. Nevertheless, the missing data within the signal leads to significant estimation error of the mode damping, giving incorrect stability analysis results. On the other hand, considering wideband instabilities in the power electronic-based power systems, the oscillation signals are heterogeneous, containing components of different frequencies and damping. The existing empirical mode decomposition (EMD)-related algorithms can decompose the complex signal into multiple intrinsic mode functions (IMF) [28], as shown in Fig. 1. However, due to its frequency-opaque decomposition characteristics and lack of strict mathematical justification, the frequency boundaries of each IMF cannot be determined, resulting in inexplicit decomposition.

To this end, a viable improvement is to combine the translation and scaling of the time window to process signals at different frequency and time resolutions simultaneously, known as multi-resolution analysis (MRA) and commonly used in the wavelet transform (WT) [29]. In this paper, an advanced method based on multi-resolution dynamic mode decomposition (MR-DMD) [30] is leveraged for wideband instability mode identification and oscillation component extraction, by combining DMD with MRA. It has strong robustness against non-stationary nonlinear features of transient variations, while multi-level time-domain signal decomposition with explicit frequency boundaries of each level can be achieved. Furthermore, in analogy with the impact of the wavelet basis function on WT, key parameters significantly affect the performance of MR-DMD, while there are different identification requirements in different frequency ranges for the wideband oscillation issues of grid-tied converters. However, the MR-DMD proposed in previous studies [30] did not consider the impact mechanism and the optimal design of algorithm parameters. Therefore, it is necessary to build an application framework for MR-DMD with parameter design to maximize the algorithm performance. The key contributions of this paper are as follows:

1) MR-DMD is leveraged in the realm of wideband oscillation identification of grid-connected converter systems for the first time to accurately identify dominant oscillation modes, showing excellent robustness against missing data.
2) The impact of key parameters on algorithm performance is revealed through derivation, and then an overall application framework of MR-DMD involving parameter design is proposed to optimize identification abilities over low/high-frequency ranges and specify decomposition boundaries to extract different oscillation components.
3) Based on the identified eigenvalues and extracted oscillation components in different frequency ranges, MR-DMD is utilized to implement clear damping assessment, instability prediction, and filtering functions with settable cutoff frequencies.

The rest of this paper is organized as follows. Section II describes the research scenarios and introduces the MR-DMD-based method with its drawbacks. Section III proposes an application framework of MR-DMD after the derivation of key algorithm parameters, and Section IV presents verification and comparison of the methods. Finally, Section V gives the conclusions.

II. SYSTEM DESCRIPTION AND BASIC METHOD

A. Mode Identification of Wideband Instability

The crucial point of wideband oscillation mode identification based on measured signals is dominant eigenvalue extraction in different frequency ranges while capturing inherent properties such as oscillation amplitude and damping to assess instability. The robustness should also be considered such as the impact of missing data in the sampled signal.

In this paper, two typical instability phenomena in different grid-tied converter systems shown in Fig. 2 are used as the study cases. When low-frequency oscillation (LFO) occurs in, e.g. electrified railways featuring a single-phase rectifier of the electric train using transient direct current control (TDCC) [31], there is an oscillating component in the DC voltage v_{dc} with a frequency of f_{LFO}, which is generally lower than 10 Hz [3]. When high-frequency resonance (HFR) occurs in a three-phase inverter system of renewable energy source using grid-forming (GFM) control scheme [7], there is a harmonic component below the Nyquist frequency in the AC voltage signal v_c (Fig. 2(d) shows phase "a" of v_c denoted as v_{ca}).

B. DMD Algorithm

As a mode identification method, DMD can extract exact DMD modes using snapshots of measurement data.

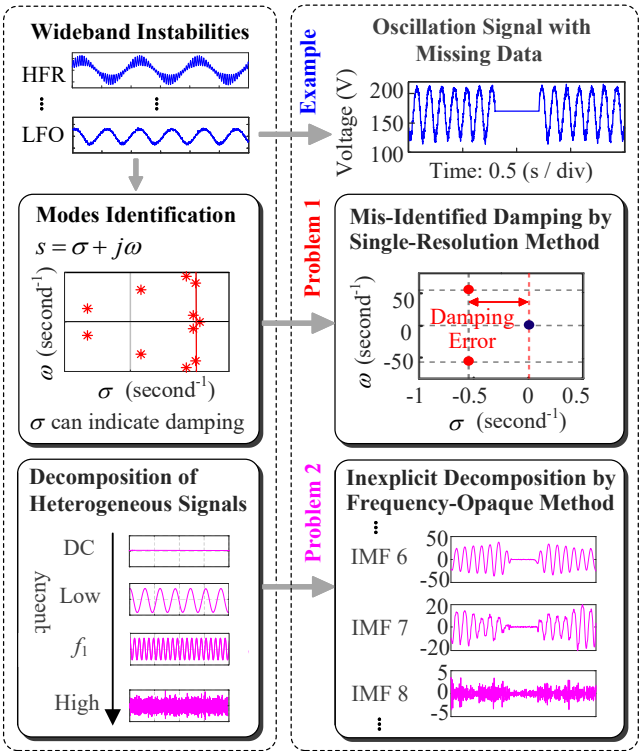

Fig. 1. Problems and shortcomings of existing methods for accurate mode identification and signal decomposition. (HFR: High-Frequency Resonance, LFO: Low-Frequency Oscillation, f_1: Fundamental Frequency)

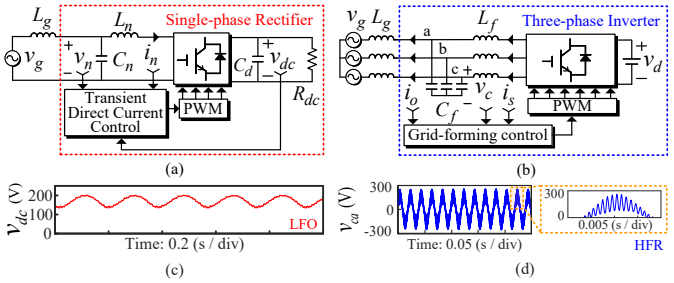

Fig. 2. System diagram and instability issues of grid-tied converters — (a) single-phase rectifier where (c) low-frequency oscillation occurs, and (b) three-phase inverter where (d) high-frequency resonance occurs

Based on discrete-time measurements, it is assumed that $x_{i,j(i=1,2,...,m;\ j=1,2,...,n)}$ denotes an element of the measurable discrete system states, where m is the total number of spatial system states, and n is the total number of temporal iterations with regular sampling time interval Δt. The data snapshot at the j^{th} sampled point is defined as $\mathbf{x}_j = (x_{1,j}, x_{2,j}, ..., x_{m,j})^T$. By gathering the snapshots, a pair of data matrices with a time shift are generated as $\mathbf{X}_1^{n-1} \in \mathbb{R}^{m\times(n-1)} = [\mathbf{x}_1, \mathbf{x}_2, ..., \mathbf{x}_{n-1}]$ and $\mathbf{X}_2^{n} \in \mathbb{R}^{m\times(n-1)} = [\mathbf{x}_2, \mathbf{x}_3, ..., \mathbf{x}_{n}]$ with their mapping relationship given as:

$$\mathbf{X}_2^n = \mathbf{A}\mathbf{X}_1^{n-1} \tag{1}$$

where, $\mathbf{A} \in \mathbb{R}^{m\times m}$ is the state matrix containing the inherent dynamics in the measured data. Thus, the DMD algorithm aims to find a best-fit approximation of $\mathbf{A}$ for mode identification [23]–[25]. Singular value decomposition (SVD) with the truncation rank r is implemented to obtain a reduced-order matrix $\tilde{\mathbf{A}}$, and the eigen-decomposition (ED) of $\tilde{\mathbf{A}}$ is calculated to extract the eigenvalue matrix $\mathbf{\Lambda} = diag\begin{bmatrix}\lambda_1 & \lambda_2 & \cdots & \lambda_r\end{bmatrix}$. Furthermore, the eigenvectors $\mathbf{\Phi}$ of original state matrix $\mathbf{A}$ can be approximated, and there is $\mathbf{A} = \mathbf{\Phi}\mathbf{\Lambda}\mathbf{\Phi}^{-1}$. On this basis, the discrete signal can be reconstructed and predicted as:

$$\mathbf{x}_{j+1} = \mathbf{\Phi}\mathbf{\Lambda}\mathbf{\Phi}^{-1}\mathbf{x}_j = \mathbf{\Phi}\mathbf{\Lambda}^j \underbrace{\mathbf{\Phi}^{-1}\mathbf{x}_1}_{\mathbf{b}} = \sum_{k=1}^{r} \mathbf{\Phi}_k(\lambda_k)^j b_k \tag{2}$$

where, $\mathbf{b} = \mathbf{\Phi}^{-1}\mathbf{x}_1$ is defined as mode amplitude, and $\mathbf{x}_1$ is the initial snapshot of measured states at time $t_1 = 0$, so the initial state of the reconstructed signal is $\mathbf{\Phi}\mathbf{\Lambda}^0\mathbf{\Phi}^{-1}\mathbf{x}_1 = \mathbf{x}_1$. Furthermore, the time-domain expression of the reconstructed signal can be given as:

$$\begin{cases} \mathbf{x}(t_j) = \sum_{k=1}^{r} \mathbf{\Phi}_k e^{\omega_k t_j} b_k = \mathbf{\Phi} e^{\mathbf{\Omega} t_j}\mathbf{b} \\ \mathbf{X}_{(t)}^{rec} = [\ \mathbf{x}(t_1) \quad \cdots \quad \mathbf{x}(t_j) \quad \cdots \quad \mathbf{x}(t_n)\ ] \end{cases} \tag{3}$$

where, $\mathbf{\Omega}$ is a diagonal matrix of continuous eigenvalues ω_k, and the relationship between the discrete eigenvalue λ_k and continuous eigenvalue ω_k is [24]:

$$\omega_k = \ln(\lambda_k)/\Delta t \tag{4}$$

where, Δt is the sampling time interval.

Moreover, the integral contribution (IC) reflecting the importance of each eigenvalue can be calculated to find the dominant mode [32], shown as:

$$\eta_i = \Delta t \left\|\mathbf{\Phi}_i\right\|_F^2 \sum_{j=1}^{n} \left|(\lambda_i)^j b_i\right| \tag{5}$$

where, η_i is the IC of the i^{th} eigenvalue, and $\|\cdot\|_F$ is the Frobenius norm.

C. MR-DMD Algorithm

Inspired by the concept of multi-resolution analysis used in the wavelet theory [29], MR-DMD applies DMD recursively in different data subsets, called the time-bins with varying timescales. As shown in Fig. 3, an oscillation mode can be considered a slow mode, if it has a relatively low frequency and slow growth/decay rate, i.e., the corresponding eigenvalue is close to the origin of the complex plane. Accordingly, after performing DMD on the available dataset (time-bin), all slow modes are screened, where the DMD approximation is constructed from the slow modes. Then, this approximation is removed from the available dataset, while the remaining part representing fast modes is split in half, obtaining two equal time-bins. The aforementioned steps are repeated recursively for each time-bin until a desired truncation level is achieved.

To be specific, according to the recursion process of MR-DMD, if the index of decomposition level is denoted as $l = 1, 2, ..., L$ (L being the termination level), the total number of time-bins in the l^{th} level can be expressed as:

$$B_l = 2^{(l-1)} \tag{6}$$

The index of time-bins in each level is denoted as $b = 1, 2, ..., B_l$, where the size of each time-bin in the l^{th} level is given by:

$$S_l = n/B_l \tag{7}$$

where, n is the total number of initial sampling points. As shown in Fig. 3, any variable in the b^{th} time-bin of the l^{th} level is marked with the superscript (l, b).

Since only the slow modes are captured, data in each time-bin need to be subsampled with a fixed number denoted as μ to improve the computational efficiency, which also makes the maximum frequency of capturable modes increase as the decomposition level increases. For slow mode screening, when a discrete eigenvalue identified by MR-DMD meets the requirement shown in (8), it can be regarded as a slow mode.

$$\left|\ln[\lambda_k^{(l,b)}]\right| \leq \rho \tag{8}$$

where, ρ is defined as the screening threshold of slow modes. By combining (3) with (8), the data matrix with only slow modes $\mathbf{X}_{slow}^{(l,b)}$ in each time-bin of each level can be reconstructed and then removed to obtain the remaining fast part as $\mathrm{X}_{fast}^{(l,b)} = \mathbf{X}^{(l,b)} - \mathbf{X}_{slow}^{(l,b)}$, which will be sent to the next level and equally split into two time-bins. After that, the same process is executed in these two time-bins recursively until reaching the truncation level L.

D. Importance of Parameter Design

MR-DMD is a recursive implementation of the DMD algorithm over multiple decomposition levels, which has two core improvements. Firstly, since the dataset is split into multiple time-bins, DMD will be executed B_l times in the l^{th} level and there are B_l eigenvalues corresponding to each mode. The total identified eigenvalues by MR-DMD in the l^{th} level will be $r \times B_l$, where r is the number of eigenvalues identified by a single execution of DMD. Thus, a series of eigenvalues instead of a single eigenvalue brings strong robustness for MR-DMD in identifying transient time behaviors or missing data. Fig. 4(a) shows an example of the mode identification of LFO based on DC voltage v_{dc}. DMD can identify the dominant mode at around 8.6 Hz with critical damping, but if a part of the data is missing, there is a significant damping error. In comparison, the dominant mode identified by MR-DMD corresponds to eight eigenvalues near the imaginary axis (the dominant mode is identified at the 4^{th} level in this case, so $B_4 = 2^3$ according to (7)). Even if the original dataset contains missing data, only the eigenvalues of the corresponding time-bin drift, while the remaining eigenvalues still maintain the correct frequency and damping properties.

Secondly, as shown in Fig. 4(b), the multi-level decomposition in terms of frequency provides modes identification in different frequency bands with corresponding reconstructed signals, and the total signal reconstruction can be achieved by stacking all levels, which can also be used for oscillation components extraction or low/high/band-pass filter by stacking some specific levels.

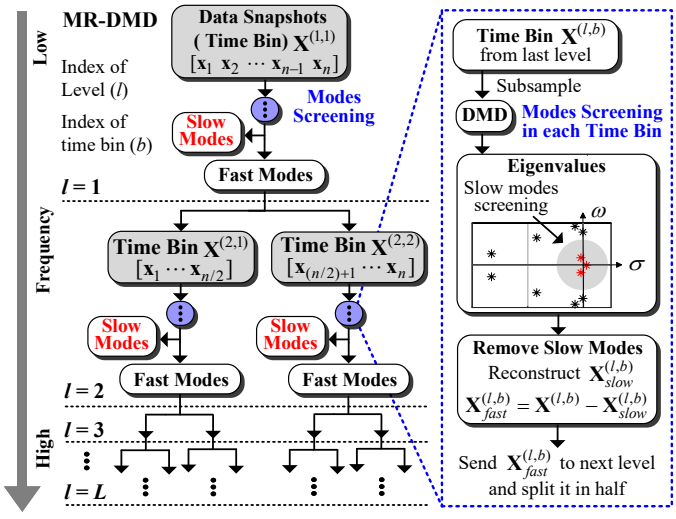

Fig. 3. Schematic of multi-resolution dynamic mode decomposition (MR-DMD) — DMD is performed recursively in varying time scales and slow modes are screened in each level.

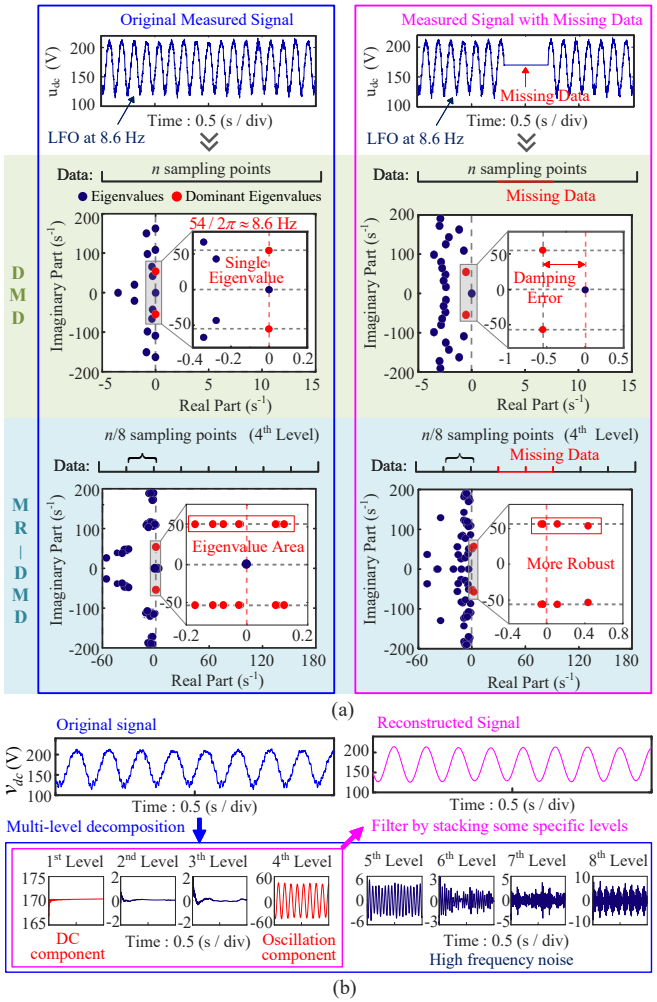

Fig. 4. Strengths of multi-resolution dynamic mode decomposition (MR-DMD) — (a) Robustness against transient variations (b) Multi-level frequency decomposition.

However, the frequency boundary of capturable modes in each level is a critical factor governing the performance of MR-DMD, which is related to key parameters. For example, in the case shown in Fig. 4, if the dominant mode at a frequency of around 8.6 Hz is identified in the 1^{st} level with only one time-bin ($B_1 = 2^0$) rather than the 4^{th} level with eight time-bins, the advantage of strong robustness will be lost. In addition, it is expected that the oscillation components within the desired frequency band can be distinguished and extracted

exactly. In other words, the filtering capability is expected to have a settable cutoff frequency. As a result, when it comes to wideband oscillation identification and oscillation component extraction in grid-tied converter systems, it is important to formulate a guidance framework for parameter design and algorithm application.

III. Proposed Framework of MR-DMD

A. Derivation of Key Algorithm Parameters

1) Fixed Subsample Number of Each time-bin (μ): The construction process of the original data matrix as stated in Section II-B shows the measured signal is sampled with regular time interval Δt. The sampling window duration of the original data matrix can be denoted as $N = n\Delta t$, where n is the total number of initial sampling points, and the initial sampling frequency f_s is:

$$f_s = 1/\Delta t = n/N \tag{9}$$

The time window duration of each time-bin in the l^{th} level (D_l) can be derived by combining with (6) and (7) as:

$$D_l = N/B_l = S_l \Delta t \tag{10}$$

Then, the subsample frequency f_l^{sp} and the maximum frequency of capturable modes f_l^{max} in the l^{th} level can be calculated based on the Nyquist sampling theorem as:

$$f_l^{max} = \frac{f_l^{sp}}{2} = \frac{\mu}{D_l} = \frac{\mu}{S_l \Delta t} = 2^{(l-2)} \frac{\mu}{N} \tag{11}$$

It can be seen from (11) that f_l^{max} increases as l increases and f_l^{max} can be set by adjusting the subsample number μ.

2) Termination Level (L): The size of time-bins in the highest level S_L must be larger than μ, otherwise the sub-sampling will fail to perform. Thus, combining with (6) and (7), the limitation of the termination level L is expressed as:

$$\mu \le S_L = \frac{n}{B_L} = \frac{n}{2^{(L-1)}} \tag{12}$$

$$L \le \log_2 [n/\mu] + 1 \tag{13}$$

3) Screening Threshold of Slow Modes (ρ): Since slow modes are some modes closer to the origin of the complex plane among all the capturable modes, it is assumed that the relationship between the maximum frequency of all capturable modes (f_l^{max}) and slow modes (f_l^{slow}) in the l^{th} level is:

$$f_l^{slow} = f_l^{max}/g \tag{14}$$

where, g is a constant rational number larger than 1.

The imaginary part of a continuous eigenvalue divided by 2π is the mode oscillation frequency, so (14) is rewritten as:

$$\frac{\left|\mathrm{Im}[\omega_l^{slow}]\right|}{2\pi} = \frac{f_l^{max}}{g} \tag{15}$$

where, ω_l^{slow} is the continuous eigenvalue corresponding to the slow mode with maximum frequency in the l^{th} level.

After sub-sampling, the relationship between the discrete and continuous eigenvalues shown in (4) can be re-written by combining with (11) as:

$$\omega_k = \frac{\ln({\lambda_k}^{\mu/S_l})}{\Delta t} = \frac{\mu \ln(\lambda_k)}{S_l \Delta t} = 2 f_l^{max} \ln(\lambda_k) \tag{16}$$

Obviously, (16) holds for all identified eigenvalues including ω_l^{slow}, thereby (17) is obtained as:

$$\omega_l^{slow} = 2 f_l^{max} \ln(\lambda_l^{slow}) \tag{17}$$

The key under/negative-damping eigenvalues corresponding to slow modes are located near the imaginary axis, indicating their real parts are much smaller than imaginary parts, so there is $\left|\mathrm{Im}[\omega_l^{slow}]\right| \approx \left|\omega_l^{slow}\right|$. As a result, (18) is derived by substituting (17) into (15), as follows:

$$\left|\ln(\lambda_l^{slow})\right| = \pi/g \tag{18}$$

Since λ_l^{slow} is the discrete eigenvalue corresponding to the slow mode with maximum frequency in the l^{th} level,it can be found by comparing (18) with (8) that $\rho = \pi/g$.

Fig. 5 gives a case showing all identified eigenvalues (modes) and screened slow modes in the l^{th} level, where ρ is set as π /4 (i.e., $g = 4$, and $f_l^{slow} = f_l^{max}/4$). Eigenvalues with frequencies lower than f_l^{slow} are regarded as slow modes. However, some eigenvalues with frequencies lower than f_l^{slow} but far away from the real axis are not considered slow modes due to the unmet approximation of $\left|\mathrm{Im}[\omega_l^{slow}]\right| \approx \left|\omega_l^{slow}\right|$. Fortunately, they can be ignored in the oscillation identification due to their large damping.

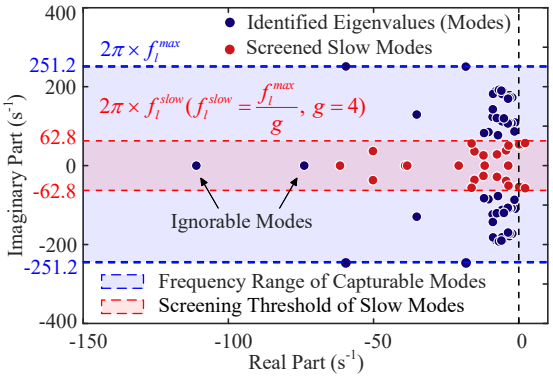

Fig. 5. Screening threshold of slow modes f_l^{slow} — modes with frequencies lower than f_l^{slow} is screened as slow modes.

B. Guidance of Parameters Setting

The parameter derivation proves that the frequency boundary of capturable modes in each level f_l^{slow} is affected by μ and g, while μ and L constrain each other. On this basis, the detailed parameterization procedure will be clarified in this section to optimize the MR-DMD algorithm performance.

By substituting (9) and (12) into (11), an inequality can be obtained as follows:

$$f_L^{max} = \frac{\mu}{2 S_L \Delta t} \le \frac{1}{2\Delta t} = \frac{f_s}{2} \tag{19}$$

Hence, the maximum frequency of capturable modes in the highest level f_L^{max} is limited by the Nyquist frequency $f_s/2$. According to (9), (11) and (19), subsample number μ should be set as (20) to minimize Δf_d (defined as the difference between f_L^{max} and $f_s/2$), i.e., maximize the use of data.

$$\mu = \left\lfloor \frac{n}{2^{(L-1)}} \right\rfloor \tag{20}$$

where "$\lfloor\rfloor$" represents rounding down.

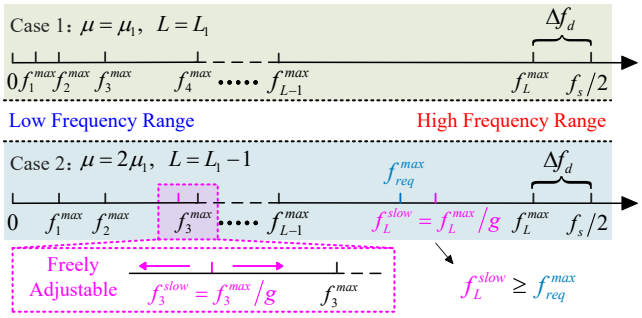

Fig. 6. Impact of different algorithm parameters on identifiable frequency ranges in each level.

So far, a series of optimal choices for μ can be obtained from (20) based on different L. When it comes to how to decide the final μ, it has been revealed that when μ increases, L must be decreased to ensure the inequality given in (12) and (13) holds, and vice versa. Two cases with different parameters are shown in Fig. 6 to clarify this conclusion, where μ in Case 2 is twice of that in Case 1, so the corresponding L is one smaller according to (12) and (13). A comparison between the two cases in Fig. 6 shows that a smaller μ will provide more decomposition levels in the low-frequency range, allowing for more robust identification of LFO. Meanwhile, a larger μ will lead to a faster approach to the high-frequency range, avoiding too many decomposition levels and large computational burdens. Thus, for wideband oscillation identifications, μ should be set as an appropriate value according to different application scenarios and frequency ranges. Once μ is selected, the corresponding L is also determined by (20).

According to (18), the setting of the screening threshold of slow modes ρ is essentially the selection of the constant g. As shown in Case 2 in Fig. 6, g has an important function to flexibly specify the identifiable frequency range of oscillation modes in different levels to separate the oscillating components with specific frequencies. Although f_l^{max} can also be designed by setting μ as shown in (11), the selection criterion of optimal μ in (20) restricts the adjustable range, so the setting of g can compensate for this limitation. It is worth mentioning that, the setting of g also comes with the side effect of decreasing the maximum frequency of capturable modes from f_L^{max} to f_L^{slow}. To ensure that all concerned modes are identified, f_L^{slow} must be larger than or equal to the maximum oscillation frequency required by the user denoted as $f_{req}^{\max}$:

$$f_{req}^{max} \leq f_L^{slow} = \frac{f_L^{max}}{g} \leq \frac{f_s}{2g} \tag{21}$$

Therefore, the screening threshold of slow modes ρ ($\rho = \pi/g$) can be set according to the required f_l^{slow}, but the optional range of g is limited by $\mathrm{g} \leq f_s/(2f_{req}^{max})$.

C. Data Pre-processing

In the DMD-based algorithm, a high-order data matrix is necessary to ensure accurate results containing all critical modes [24], [25]. The requirement of data matrix columns n is easy to fulfill, as long as high enough sampling frequency or sampling windows are available. However, since there are only a few measurement channels available in the small-scale grid-tied converter systems as shown in Fig. 2, the demand for the number of system states, i.e., rows of the data matrix m, cannot be met. To this end, a data-stacking technique based on the Hankel matrix [33] is applied to increase the rows of the data matrix. As shown in Fig. **??**, the augmented data matrices $\mathbf{X}_{aug,1}, \mathbf{X}_{aug,2} \in \mathbb{R}^{ms\times(n-s)}$ are obtained by shift-stacking operations with a higher row dimension than the original matrices $\mathbf{X}_1^{n-1}, \mathbf{X}_2^{n} \in \mathbb{R}^{m\times(n-1)}$, where s is the shift-stacking number, and the mapping relationship between two data matrices remains unchanged.

It is worth mentioning that, after the shift-stacking operation, the total number of initial sampling points (n) needs to be regarded as $n-s$, while the sampling window duration is $N = (n-s)\Delta t$. Since a large value of s increases the computational burden, while a too-small s leads to low identification accuracy, s is set to 20% of n in this paper.

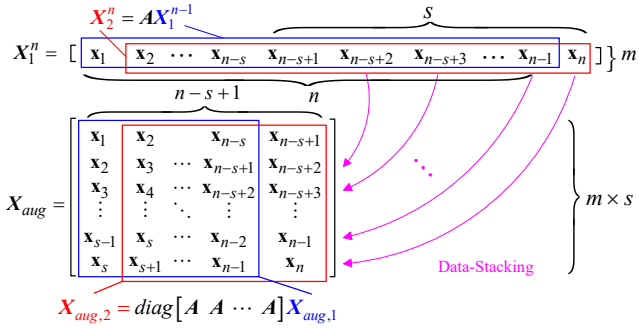

Fig. 7. Diagram of data-stacking technique — data matrices are augmented with higher row dimensions.

D. Application Framework

Based on the aforementioned derivations and analysis, a comprehensive application framework of MR-DMD for wideband oscillation identification in power converter-based systems is proposed as shown in Fig. 8. The entire framework includes three main parts, i.e., input (original data and application requirements), implementation (identifiable frequency range assessment, algorithm parameters design, and MR-DMD itself), and output (oscillation identification results).

First of all, sampling window duration N, total number of initial sampling points n, and initial sampling frequency f_s have been determined when sampling the original signal. On this basis, together with the default screening threshold constant of slow modes g (such as 4), the identifiable frequency range of the algorithm is assessed according to (21) to judge whether it is enough for the desired frequency range $f_{req}^{\max}$.

Remark 1*: If the assessment result is 'NO', increasing f_s and decreasing g are feasible solutions. However, if there is also a demand for freely adjustable f_l^{slow} realized by setting g, only increasing f_s can be chosen. If there is no specific demand for $f_{req}^{\max}$, this step can be skipped.*

The data-stacking step is then performed based on the elaboration in Section III-C. For parameter design, the selection list of subsample number μ is obtained from (20) by maximizing the identifiable frequency range, among which the optimal value of μ is determined depending on the specific application scenario, and the corresponding termination level L can be calculated. Since μ is the column number of the data matrix in each time-bin, it cannot be too small due to the limitations

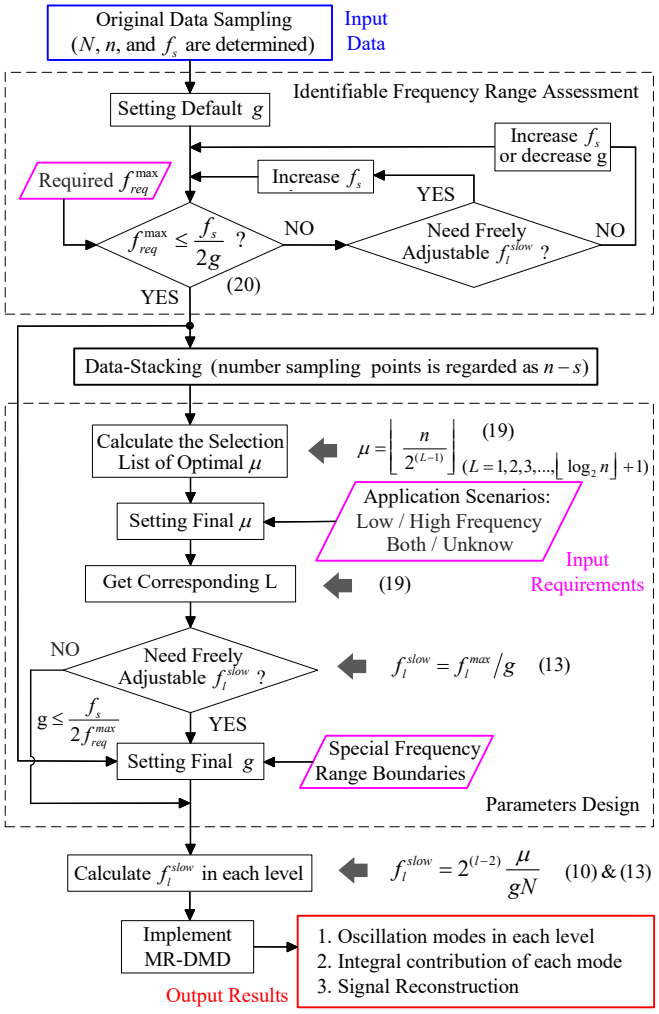

Fig. 8. Application framework of MR-DMD algorithm for wideband oscillation identification in power electronic converter-based system.

stated in Section III-C. Identifiable frequency boundaries can be set by tuning g if the specific oscillation components need to be separated, where the adjustable range of g is limited by (21). Finally, the MR-DMD outputs the results.

***Remark II**: With properly designed parameters, algorithm performance is improved in terms of robustness, maximum identifiable range, and flexible setting of frequency boundaries in each level for specific oscillation component extraction.*

IV. Experimental Tests And Validations

A. Dataset Collection and Parameter Settings

To validate the effectiveness of the MR-DMD-based identification method and the proposed application framework for wideband oscillation mode identification, offline and online tests are performed with the down-scaled experimental platforms as shown in Fig. 9. The experimental setups are built according to the system configurations and control strategies shown in Fig. 2, where the plants of the single-phase rectifier and three-phase inverter are implemented based on the Imperix PEB-8024 SiC modules, the control strategies are performed on the B-BOX RCP control device, and experimental waveforms can be monitored and saved by the software named Cockpit. The main system parameters are listed in Table II.

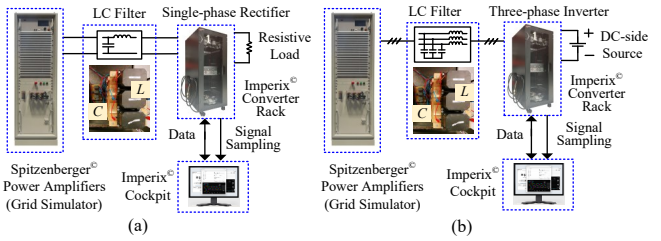

Fig. 9. Experimental setup of down-scaled grid-tied (a) single-phase rectifier and (b) three-phase inverter.

TABLE II
Main Parameters of Experimental Setup

Parameter	Description	Value
v_g	Nominal AC voltage	110 V, 50 Hz
L_g	Grid-side inductance	8 mH
L_n, L_f	LC filter inductance	4 mH
C_n, C_f	LC filter capacitance	10 uF
v_d	DC voltage of the inverter	400 V
v_{dc}	DC voltage of the rectifier	170 V
R_d	Load resistance	460 Ω
C_d	DC-side capacitance	800 uF
f_{sw}	Switching frequency	20 kHz

For the offline test, datasets are collected during oscillation events. Under the LFO scenario, the dataset is collected from the experimental platform shown in Fig. 9(a) when a LFO at 5.3 Hz occurs. DC voltage v_{dc} is used as the measured signal in a sampling window of 2 seconds ($N = 2$), and the sampling frequency f_s is 2500 Hz, so $n = 5000$. To test the algorithm robustness, the 1000^{th} to 2000^{th} and 3000^{th} to 4000^{th} sampling points are set as missing data, supplemented by the reference value of $v_{dc} = 170$. According to the proposed application framework of MR-DMD shown in Fig. 8, if the default of g is set as 4, the identifiable frequency range (312.5 Hz) is well beyond $f_{req}^{\max}$ (10 Hz). Then, the data stacking technique with shift-stacking number s of 1000 is employed to generate an augmented data matrix (1000×4000), so now $n = 4000$, and $N = 1.6$ seconds. Next, a selective list of the subsample number μ is obtained as (4000, 2000, 1000, 500, 250, 125, 62, 31, 15, 7, 3, 1), in which μ is finally determined as 15 for the robust identification of low-frequency modes, while the corresponding L is calculated as 9. It is expected to separate the low-frequency modes with frequencies below 10 Hz, which can be achieved by adjusting g to 7.5 (within the adjustable range $g \le 125$). Based on the designed parameters, frequency boundaries f_l^{slow} in each level can be calculated by (11) and (14), as shown in Table III.

Under the HFR scenario, when HFR at around 1.4 kHz occurs in the experimental platform shown in Fig. 9(b), the phase "a" of AC voltage v_{ca} is used as the measured signal in a sampling window of 0.25 seconds, and sampling frequency is 20 kHz (i.e., f_s = 20 kHz, $N = 0.25$ and $n = 5000$), where the 1000^{th} to 2000^{th} and 3000^{th} to 4000^{th} sampling points are set as missing data, supplemented by 0. Similarly, the parameterization of MR-DMD follows the steps in the proposed framework. After identifiable frequency range assessment (f_L^{slow} is capped at 2.5 kHz when setting g as the default of 4) and data stacking operation ($s = 1000$, so $n = 4000$ and $N = 0.2$), the list of optimal μ is obtained as (4000, 2000, 1000, 500, 250, 125, 62, 31, 15, 7, 3, 1). The final μ is set as 31 considering the robust identification of

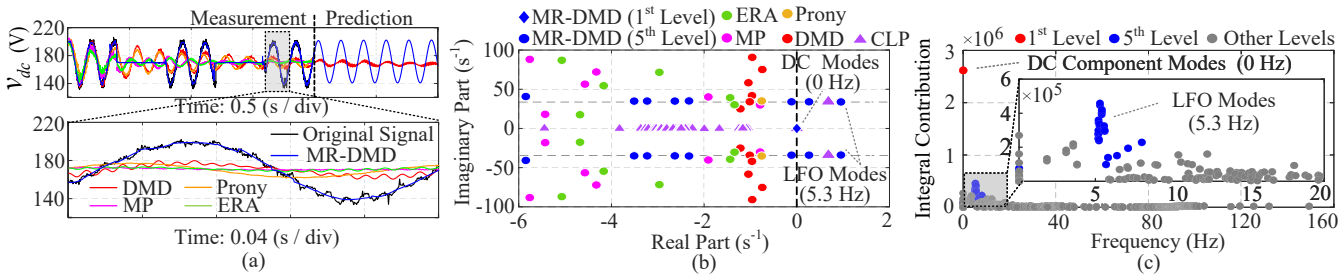

Fig. 10. Robustness comparison of mode identification algorithms for low-frequency oscillation (LFO) — (a) Signal reconstruction and prediction (b) Identified modes (c) Integral contribution of each mode identified by MR-DMD.

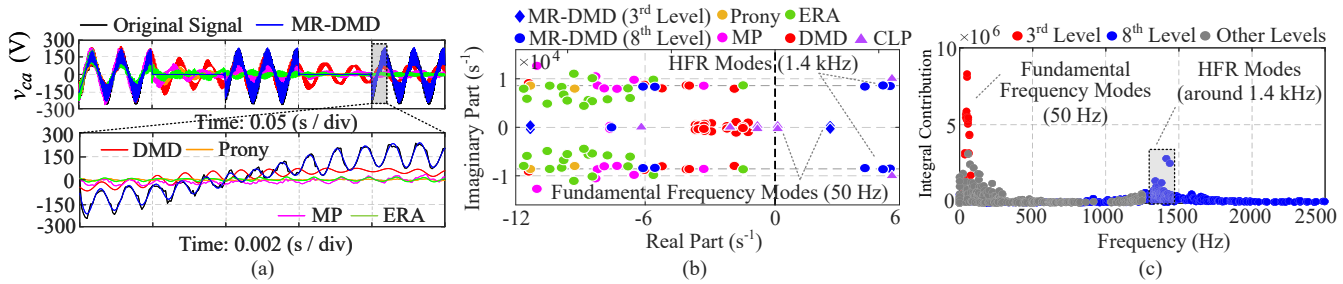

Fig. 11. Robustness comparison of mode identification algorithms for high-frequency resonance (HFR) — (a) Signal reconstruction (b) Identified modes (c) Integral contribution of each mode identified by MR-DMD.

fundamental-frequency modes (50 Hz), then L is calculated as 8. Since there is no demand for special frequency boundaries, g is kept as the default of 4. Finally, f_l^{slow} in each level can be derived as shown in Table III.

TABLE III
MAXIMUM IDENTIFIABLE FREQUENCIES IN EACH DECOMPOSITION LEVEL WITH DESIGNED PARAMETERS

Indicators	**Values**								
Designed Parameters (LFO)	μ = 15, L = 9, g = 7.5, N = 1.6								
Level (l)	1	2	3	4	5	6	7	8	9
f_l^{slow} (Hz)	0.6	1.2	2.5	5	10	20	40	80	160
Designed Parameters (HFR)	μ = 31, L = 8, g = 4, N = 0.2								
Level (l)	1	2	3	4	5	6	7	8	–
f_l^{slow} (Hz)	19.4	38.8	77.5	155	310	620	1240	2480	–

B. Robust Damping Assessment and Instability Prediction

For the original LFO signal measurement containing nonlinear and non-stationary features such as missing data shown in Fig. 10(a), the performance of different mode identification algorithms is compared. Fig. 10(b) shows the identified modes in the low-frequency range, where the mode frequency can be calculated by dividing the corresponding imaginary part value by 2π, and positive/negative real part values indicate negative/positive damping. It can be seen from Fig. 10(b) that existing Prony, MP, ERA, and DMD algorithms fail to identify low-frequency oscillation modes with accurate frequency and critical/negative damping when the collected dataset contains missing data. However, MR-DMD is still able to identify low-frequency oscillation modes with a frequency of 5.3 Hz and negative damping, matching the closed-loop poles (CLP) extracted from the analytical transfer function model of the grid-tied single-phase rectifier system. It is worth mentioning that, as a model-free identification algorithm, MR-DMD is mainly used to identify dominant modes with critical/negative damping based on sampled signals, which are sufficient to detect oscillation issues. Furthermore, the integral contribution (IC) calculated by (5) can reflect the importance of each mode identified by MR-DMD, as shown in Fig. 10(c), which verifies the modes with a frequency of around 5.3 Hz in the 5$^{\text{th}}$ level are the dominant modes. Correspondingly, the reconstructed signal by MR-DMD aligns closely with the original signal as shown in Fig. 10(a), but other algorithms cannot achieve an accurate signal reconstruction.

The damping assessment of the modes identified by the MR-DMD can be used for stability analysis. According to Fig. 10, low-frequency modes in the right half plane with the frequency of 5.3 Hz are dominant negative damping modes, indicating the unstable state with the occurrence of LFOs at 5.3 Hz. Moreover, using DMD-based algorithms, not only signal reconstruction but also prediction can be achieved according to (3). As shown in Fig. 10(a), a continuous large oscillation is predicted correctly by the MR-DMD, but DMD incorrectly predicts the rapid decay of the oscillations due to the damping error of the identified low-frequency oscillation modes. It is worth mentioning that the prediction by MR-DMD is realized based on the last time-bin of each level, and the high-frequency components in the signal cannot be accurately predicted due to the minor size of the time-bin in several top levels, so there is only low-frequency component in the predicted signal without high-frequency noise as shown in Fig. 10(a).

As shown in Fig. 11(a), the original HFR signal with missing data and reconstructed signals by different identification algorithms are compared, where MR-DMD can reconstruct the original signal accurately due to its exact identification of fundamental frequency mode at 50 kHz in the 3$^{\text{rd}}$ level and high-frequency oscillation modes at around 1.4 kHz with negative damping in the 8$^{\text{th}}$ level as shown in Fig. 11(b). The identified eigenvalues by MR-DMD almost match the closed-loop poles (CLP) extracted from the analytical transfer function model of the grid-tied three-phase inverter system with admissible

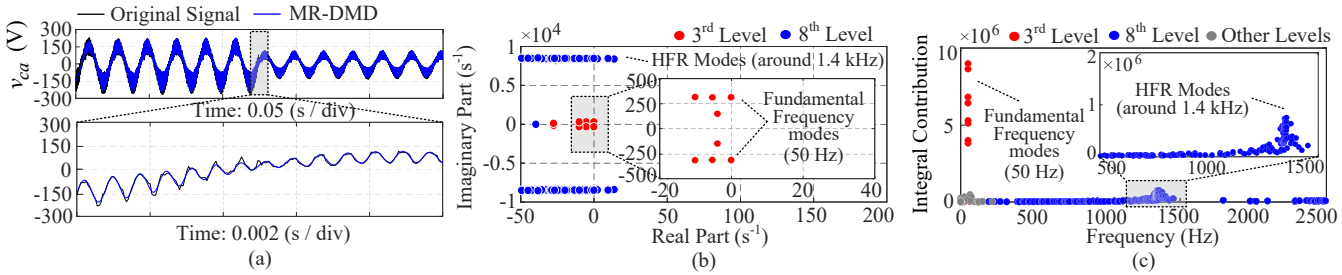

Fig. 12. Robust performance of MR-DMD algorithms under the voltage sags scenario — (a) Signal reconstruction (b) Identified modes (c) Integral contribution of each mode identified by MR-DMD.

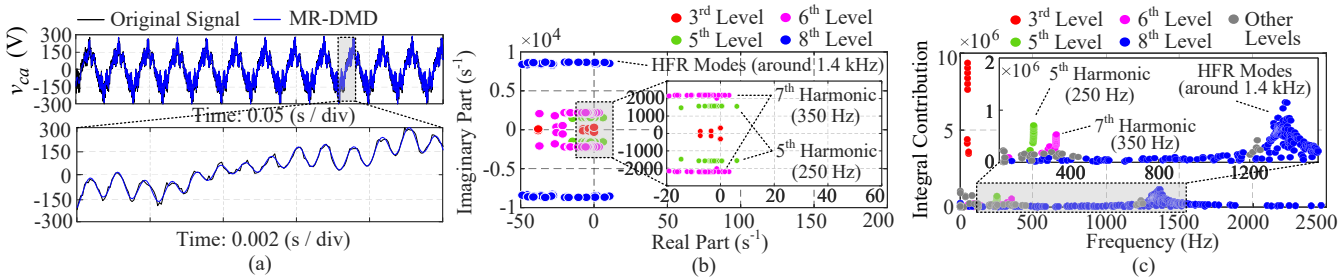

Fig. 13. Robust performance of MR-DMD algorithms under the harmonic distortion scenario — (a) Signal reconstruction (b) Identified modes (c) Integral contribution of each mode identified by MR-DMD.

errors. However, other identification algorithms fail to reconstruct the original signal, while the high-frequency oscillation modes are identified with large damping errors. In addition, the calculation of IC in Fig. 11(c) verifies the identified high-frequency modes and fundamental frequency modes are the dominant modes. Similarly, the damping assessment can be used for stability analysis, indicating the unstable state with the occurrence of HFRs at 1.4 kHz, but the signal prediction is not given in Fig. 11(a) since it is not applicable to high-frequency components in the signal.

In addition to missing data, more potentially realistic scenarios in terms of identification robustness of the MR-DMD algorithm are considered, with the same HFR data and algorithm parameters used in Fig. 11. It can be seen from Fig. 12 that, if the sampled voltage signal sags to half of its original value at the midpoint of the sampling window, MR-DMD can still identify the dominant HFR modes at around 1.4 kHz and fundamental frequency modes, while the sampled signal can be reconstructed accurately, unaffected by the sampled signal sags. To verify the harmonic distortion immunity of the MR-DMD algorithm, the fifth harmonic and seventh harmonic with an amplitude of 30 volts are superposed to the original sampled signal. Fig. 13 shows that the identification accuracy of MR-DMD for original HFR modes and fundamental frequency modes will not be affected by harmonic distortion, while the corresponding harmonic modes can also be extracted in the different decomposition levels, matching the frequency boundary computation results as shown in Table III.

In the practical application of mode identification methods, the computation speed of extracting mode damping and frequency information is a significant evaluation indicator. In the cases of the number of original sampling points n equal 5000, 4000, 30000, and 2000 respectively, the comparison of the computational time (from reading data to outputting mode information) of MR-DMD and other mode identification algorithms is shown in Table IV, in which the algorithms are performed on the host computer with Intel(R) Core(TM) i5-1135G7 @2.40GHz, 16.0 GB(RAM), and 64-bit operating system. It can be seen that, although MR-DMD is the recursive implementation of DMD, the computation speed of MR-DMD is instead faster with larger data sizes due to the subsampling in each time-bin, while the computation time of all algorithms increases as the data size increases. Further improvement of computation speed for rapid oscillation detection is one of the future scopes of this paper.

TABLE IV
COMPUTATION TIME OF MODE IDENTIFICATION ALGORITHMS

Algorithms		MR-DMD	DMD	Prony	ERA	MP
Computation Time (s)	n = 5000	0.3643	0.8475	0.6714	0.4231	0.7455
	n = 4000	0.3127	0.6712	0.5075	0.3324	0.6272
	n = 3000	0.1812	0.2062	0.3814	0.2149	0.2474
	n = 2000	0.1028	0.1045	0.2485	0.1061	0.1624

C. Configurable Signal Decomposition and Filtering

The LFO signal reconstructed by MR-DMD shown in Fig. 10(a) is the final result after stacking all levels, but the signal reconstruction is separately implemented in multiple levels with different frequency bands as shown in 14(a). It can be seen that 1st level determines the DC component of the signal (0 Hz), and 5th level extracts the main low-frequency oscillation component (5.3 Hz), matching the calculation results in Table III and mode identification results shown in Fig. 10(b). Other levels just provide further fine-fitting such as high-frequency noise. The frequency boundaries of each level are specified by designed parameters, so low/high/band-pass filters with well-defined cutoff frequencies can be realized by stacking specific levels. For example, by stacking reconstructed signals in 1st to 5th level, a low-pass filter with a cutoff frequency of 10 Hz can be realized to extract the low-frequency components of the signal and filter out the noise.

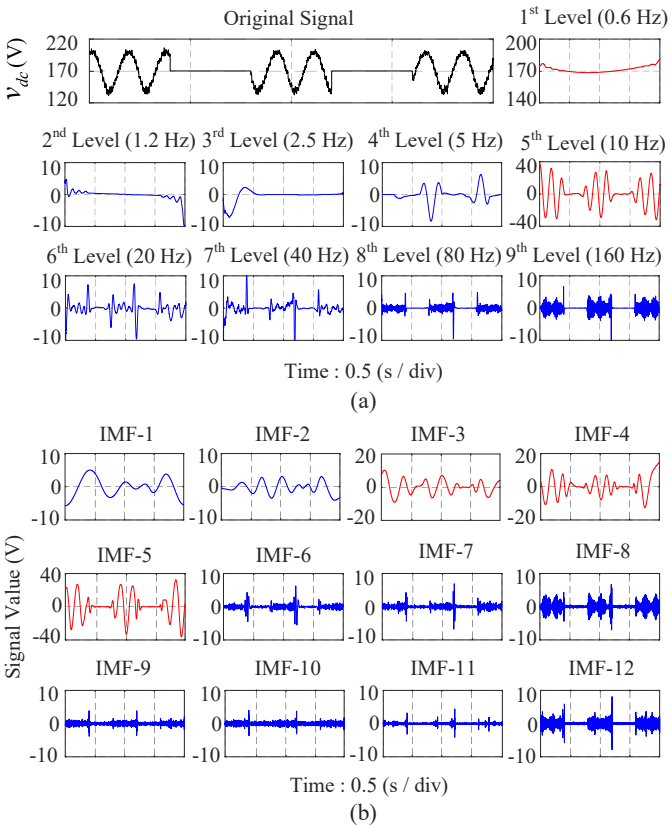

Fig. 14. Signal decomposition of low-frequency oscillation with missing data (a) using MR-DMD, (b) using complete ensemble empirical mode decomposition with adaptive noise (CEEMDAN).

The existing EMD algorithm can also decompose the complex signal into multiple intrinsic mode functions (IMF) containing features of the original signal at different frequency bands [28]. The improved version of EMD, i.e., complete ensemble EMD with adaptive noise (CEEMDAN) proposed in [34] is employed as a comparison, as shown in Fig. 14(b), where two key parameters are set appropriately (the noise standard deviation is 0.2 and the ensemble size is 500). It can be found that CEEMDAN is unable to extract the DC component of the signal, and the low-frequency oscillation component is split into 3 IMFs (IMF-3 to IMF-5) that cannot be explicitly distinguished. The decomposition number of IMF and the frequency boundaries of each IMF is unknown, which cannot be set to extract oscillation components within specific frequency ranges, so the filter function of MR-DMD with well-defined cutoff frequencies cannot be achieved by EMD-related algorithms. Moreover, EMD-related algorithms can only decompose signals into different frequency ranges, but without the oscillation mode identification capability to provide damping assessment.

The multi-level reconstruction and decomposition of the HFR signal are shown in Fig. 15, where the fundamental-frequency component (50 Hz) is extracted in the 3rd level, while the 8th level gives the main high-frequency resonance component (around 1.4 kHz), matching the calculation results of frequency boundaries in Table III and mode identification results in Fig. 11(b). Similarly, the oscillation component extraction and filtering functions can be performed by stacking specific levels. For example, by only extracting reconstructed signals in the 8th level, a band-pass filter with a cutoff frequency of 1240 Hz and 2480 Hz can be realized to extract the high-frequency oscillation components at around 1400 Hz and filter out other low-frequency components.

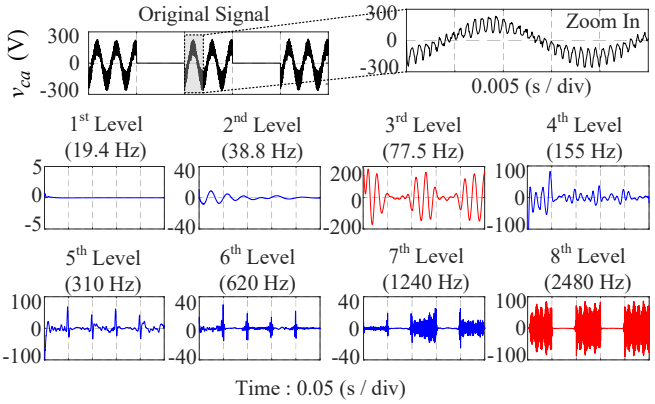

Fig. 15. Signal decomposition of high-frequency resonance with missing data using MR-DMD.

D. Necessity Verification of Parameter Design

The case study in Section IV-B/C shows that MR-DMD-based mode identification is robust against missing data, and it can set the frequency boundaries of the decomposition levels to accurately extract the oscillation components in different frequency bands. Actually, these advantages are brought by the designed parameters with the proposed framework. Regarding the case of LFO, parameter design facilitates adequate decomposition levels in the low-frequency range as shown in Table III. As a result, the LFO component at 5.3 Hz is extracted in the 5th level, where the number of time-bins is 16 calculated by (7), indicating the strong robustness according to the elaboration in Section II-D. As for the case of HFR, in addition to the robustness improvement, it can be found from Table III that the well-designed parameters make the maximum identifiable frequency of the highest level f_L^{slow} ($L = 8$) equal 2480 Hz, which minimizes the Δf_d defined in Fig. 6 and facilitates the maximum capture of high-frequency modes. Note that the upper limitation of identifiable frequency is $f_s/2g$, which equals 2500 Hz with f_s = 10 kHz and g = 4.

TABLE V
MAXIMUM IDENTIFIABLE FREQUENCIES OF EACH DECOMPOSITION LEVEL WITH STOCHASTIC PARAMETERS

Indicators	Values						
Stochastic Parameters (LFO)	μ = 50, L = 7, g = 4, N = 1.6						
Level (l)	1	2	3	4	5	6	7
f_l^{slow} (Hz)	3.9	7.8	15.6	31.2	62.5	125	250
Stochastic Parameters (HFR)	μ = 34, L = 7, g = 4, N = 0.2						
Level (l)	1	2	3	4	5	6	7
f_l^{slow} (Hz)	21.3	42.5	85	170	340	680	1360

To demonstrate the importance of parameter design, a comparison case for LFO is listed in Table V using a set of stochastic parameters that are not designed by the proposed framework (μ = 50, L = 7, g = 4). The corresponding calculations of frequency boundaries (f_l^{slow}) show that low-frequency oscillation modes at 5.3 Hz will be identified in the

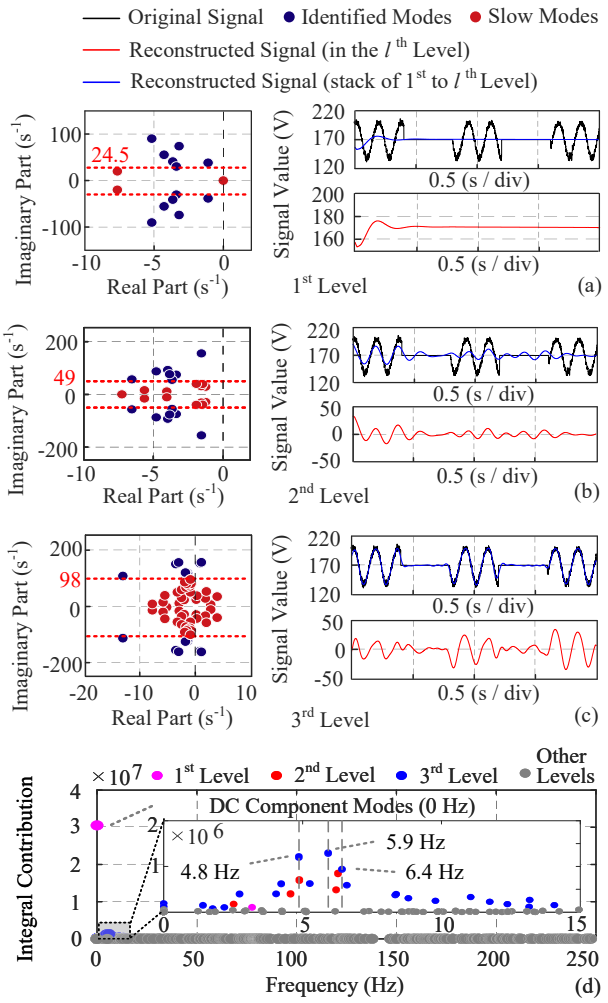

Fig. 16. Performance of MR-DMD for low-frequency oscillation mode identification and signal reconstruction using stochastic parameters — (a) in the 1st level, (b) in the 2nd level, (c) in the 3rd level, and (d) Integral contribution of all modes.

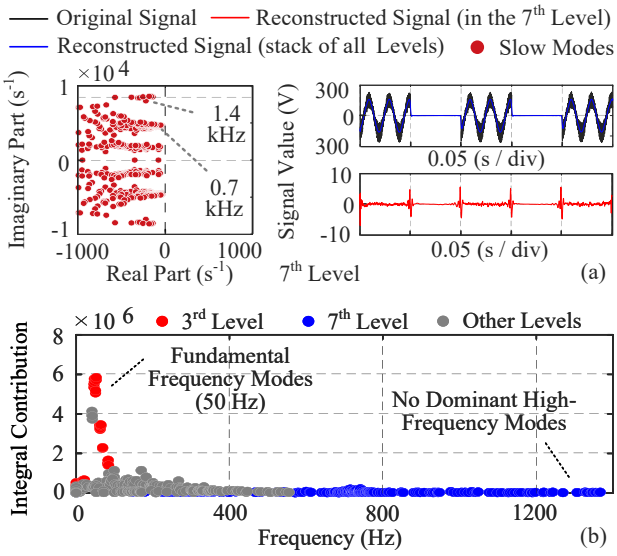

Fig. 17. Performance of MR-DMD for high-frequency resonance mode identification and signal reconstruction using stochastic parameters — (a) in the 7th level, and (b) Integral contribution of all modes.

2nd level (only 4 time-bins), which is not sufficient to obtain robustness against 2/5 missing data within the total sampling duration. As shown in Fig. 16, MR-DMD fails to identify low-frequency oscillation modes at 5.3 Hz with negative damping in the 2nd level. Instead, a large number of modes with different frequencies and negative damping are shown in the 3rd level, while it is difficult to distinguish the dominant mode by the IC in Fig. 16(d). Although the final signal reconstruction is close to the original signal, the low-frequency oscillation component at 5.3 Hz cannot be clearly distinguished and extracted. The comparison case for HFR is also listed in Table V using a set of stochastic parameters (μ = 34, L = 7, g = 4), which shows that the maximum identifiable frequency f_L^{slow} is limited to 1360 Hz, thereby failing to identify dominant high-frequency modes at 1.4 kHz with negative damping and reconstruct high-frequency resonance signal, as shown in Fig. 17.

In summary, by setting the parameters properly using the proposed framework, the advantages of the MR-DMD algorithm can be maximized, which facilitates an accurate stability analysis, oscillation component extraction, and signal filtering.

E. Online Verification

To further test the effectiveness of the MR-DMD-based identification method in the practical environment, a preliminary online test is performed as shown in Fig. 18. In which, the three-phase inverter with the GFM controller runs with the same setup as shown in Fig. 9, and the sampled data (the phase "a" of AC voltage v_{ca} is sampled with a frequency of 5 kHz) is fed into MR-DMD algorithm which is achieved in the Imperix B-BOX RCP controller with processing cores of ARM Cortex A9 1GHz 1GB DDR3. Then, the identification results can be monitored in real time and saved by the Imperix software named Cockpit.

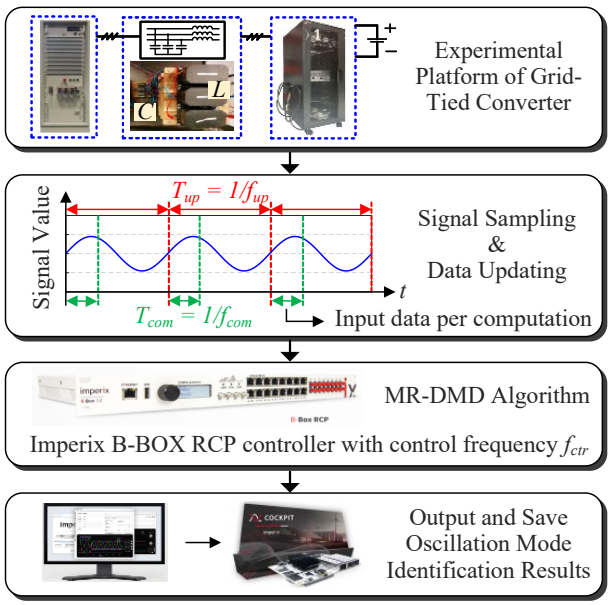

Fig. 18. Setup of online test for MR-DMD-based oscillation mode identification method (T_{up} and f_{up}: update period/frequency of identification results. T_{com} and f_{com}: sampling period/frequency of input data).

Considering the limitations of the MR-DMD calculation speed, the control frequency f_{ctr} of the Imperix B-BOX RCP

controller is set to the achievable minimum value of 50 Hz so that the device can work properly, and thus the update frequency f_{up} of the identification results is also 50Hz, i.e., the output results are updated once every 0.02 seconds. To ensure that the algorithm can complete the computation within 0.02s, 25 sampled data points are input each time, so the sampling period T_{com} of input data is 5 milliseconds. On this basis, the parameters of the MR-DMD algorithm can be derived according to the proposed application framework as μ = 5, L = 3, g = 1. The output results of MR-DMD will be updated in real time as the sampled signal changes as shown in Fig. 19, where two metrics are used to visualize the system stability assessment in numerical form, i.e., the number of identified oscillation modes with negative damping and the frequency of the most dominant mode (which has the largest integral contribution).

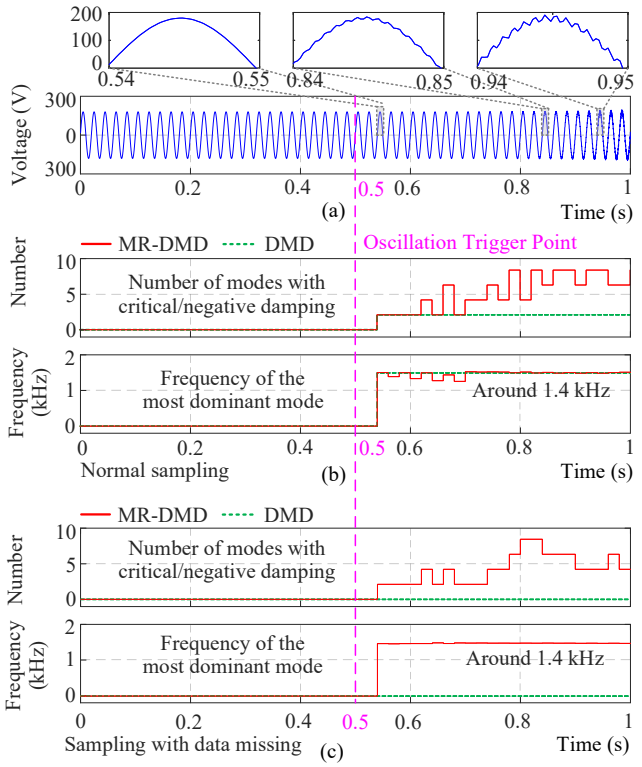

Fig. 19. Online test and comparison of DMD/MR-DMD-based oscillation mode identification — (a) Test signal, (b) Real-time identification results using normal signal sampling, and (c) Real-time identification results using signal sampling with 20% missing data.

As shown in Fig. 19(a) and Fig. 19(b), when gradually divergent high-frequency oscillation with a frequency of around 1.4 kHz is provoked at 0.5 seconds, oscillation modes with critical/negative damping can be identified within 0.04 seconds by MR-DMD before the oscillation amplitude becomes very large, while the frequency of the dominant mode is also accurately identified. As a representative of single-resolution identification methods, the online identification results of DMD are compared to highlight the advantages of MR-DMD. It can be seen from Fig. 19(b) that, DMD can only extract a pair of dominant oscillation modes (2 modes) at around 1.4 kHz, while MR-DMD can extract multiple modes due to its characteristics as mentioned in Section II-D. The total number of critical/negative damped modes identified by the MR-DMD might fluctuate due to the different signal waveforms in each time bin, but it does not affect the stability assessment results, which depends on the presence or absence of negative damped modes. As shown in Fig. 19(c), when setting the sampling window of input data with 20% missing data considering potential hardware failures in practical applications, MR-DMD can still provide accurate identification to detect the occurrence of oscillations, but the DMD fails to identify oscillation modes.

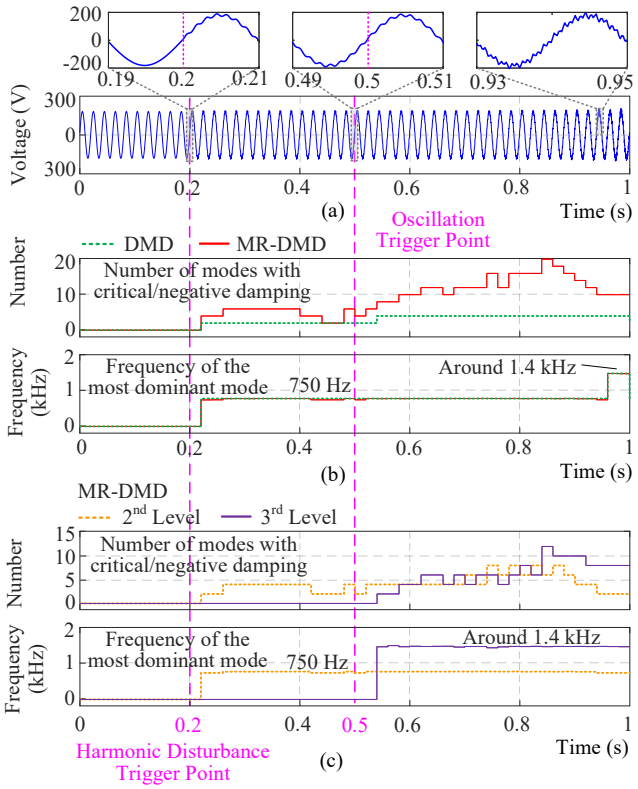

Fig. 20. Online test and comparison of DMD/MR-DMD-based oscillation mode identification considering harmonic disturbance — (a) Test signal, (b) Real-time identification using DMD and MR-DMD, and (c) Multi-level decomposition and extraction by MR-DMD

Moreover, when a 10-V 13th harmonic disturbance is set in the grid simulator from 0.2 seconds, both MR-DMD and DMD can identify the corresponding modes at 750 Hz after one update period, as shown in Fig. 20(a) and Fig. 20(b). The gradually diverging high-frequency resonance triggered at 0.5 seconds results in more negative damped modes, but due to its low initial amplitude, the high-frequency oscillation modes are not dominant until 0.96 seconds. However, since the MR-DMD is capable of multi-level decomposition, the harmonic disturbance modes at 2^{nd} level and the high-frequency oscillation modes at 3^{rd} level can be extracted separately, resulting in a clearer identification of the oscillation occurrence, as shown in Fig. 20(c).

It is worth mentioning that, due to the constraints of hardware devices and the computation speed of the algorithm, the frequency range of identifiable modes in the preliminary online test is limited. Therefore, more flexible implementation of the algorithm based on field programmable gate arrays (FPGA) and further improvement of the algorithm computation speed are the scope of future work.

V. Remarks and Discussions

In the scenarios of LFO and HFR being provoked, DC and AC voltages of grid-tied converters are sampled to verify the robust oscillation mode identification and oscillation component extraction capability of MR-DMD in this paper. However, it is worth mentioning that, in addition to accurately identifying the oscillation modes in the case of corresponding oscillations being provoked, the MR-DMD can also be applied during the stable operating states, using the response waveforms of system states after injecting a perturbation. Although the oscillation will decay with positive damping under the stable state, the identification results can reflect the potential oscillation modes of the system. Since the algorithm execution process is the same, it is not elaborated in detail here.

It has been demonstrated that the performance of MR-DMD is directly affected by the algorithm parameters. However, for the same oscillation issue, the oscillation components may be presented with different frequencies in different state signals, which can bring indirect impacts on the identification results. For example, when the LFO with a frequency of f_{os} occurs, there is an oscillation component in the DC-side voltage signal with a frequency of f_{os}, but there are two oscillation components with frequencies of $f_N \pm f_{os}$ in the AC-side voltage signal [35], where f_N is the grid fundamental frequency. Thus, with the same parameter settings, the low-frequency modes of AC side signals are located at a higher level, providing better robustness against missing data. However, it is difficult to accurately extract the two oscillation components that are symmetrical with respect to the fundamental frequency, whereas the extraction of the oscillation components is much easier when using the DC side signal. For the HFR, oscillation components with the same frequency are present in the AC and DC side signals, so the state signal selection does not affect the algorithm performance.

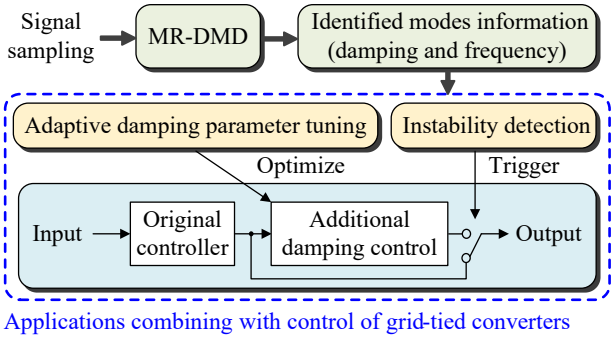

Fig. 21. Potential application scenarios of oscillation mode identification in instability detection and damping control design.

The potential application scenarios of oscillation mode identification are mainly instability detection and damping control design, as shown in Fig. 21. First, the identified mode information can be used directly to monitor the system status, and when instability is detected, mitigation measures are triggered to suppress oscillations. For example, the identified mode damping and frequency information are used in [36] for judging whether low-frequency oscillations occur in railway electrification systems, and then adjusting the operation mode to suppress the low-frequency oscillation when instability state is identified. Discrete Fourier transform is adopted in [37] to detect resonance in grid-connected inverters, and if the harmonic contents of the load current exceed the threshold, the active damping control branch will be activated. On the other hand, the identified mode information can be used for damping controller design and adaptive parameter tuning to optimize the control performance. For instance, the identified mode information by the Prony algorithm is used in [10] to calculate the parameters of the lead-lag block and determine the supplementary controller gain in the supplementary damping controller (SDC), so the designed SDC can effectively mitigate system power oscillations. Virtual impedance methods are commonly used for stability improvement [38], [39], but a fixed damping gain may affect the dynamic characteristics [40]. Therefore, adaptive tuning of control gain based on identified mode information is a potential solution. Similarly, notch filter-based active damping control has been applied for oscillation mitigation [41], but fixed-parameter notch filters are only effective for a specific frequency range, making it difficult to adapt to the instability issues over a wide frequency range in real systems. Benefiting from the frequency and damping information obtained from the identified oscillation modes, it is possible to realize adaptive parameter tuning for notch filter-based damping controls. Hence, developing an effective damping control method for wideband instability mitigation based on identified oscillation modes is one of the future scopes of this work.

VI. Conclusion

In this paper, a multi-resolution dynamic mode decomposition (MR-DMD)-based mode identification method is leveraged for identifying wideband oscillations in power converter-based systems. The MR-DMD can extract time-frequency information of oscillation modes, with the advantages of robustness and hierarchical adjustability of the identifiable frequency range. Further mathematical derivations prove that the identifiable frequency range of each level is determined by key algorithm parameters. Therefore, a holistic framework of parameter design and algorithm application is proposed considering different oscillation scenarios to improve the algorithm robustness against missing data and the maximum identifiable range, while frequency boundaries of each level can be set to realize filtering functions with defined cutoff frequencies. Based on real measurement data collected from the experimental platform, the analysis results are verified. To extend the scope of this paper, advanced optimization algorithms can be combined for adaptive parameter tuning, and identified modes can be used for damping controller design to mitigate wideband instability issues.

References

[1] H. Zhang, W. Xiang, W. Lin, and J. Wen, "Grid forming converters in renewable energy sources dominated power grid: Control strategy, stability, application, and challenges," *J. Mod. Power Syst. Clean Energy*, vol. 9, no. 6, pp. 1239–1256, 2021.

[2] F. Z. Peng, C.-C. Liu, Y. Li, A. K. Jain, and D. Vinnikov, "Envisioning the future renewable and resilient energy grids — A power grid revolution enabled by renewables, energy storage, and energy electronics," *IEEE. J. Emerg. Sel. Top. Ind. Electron.*, vol. 5, no. 1, pp. 8–26, 2024.

[3] H. Hu, Y. Zhou, X. Li, and K. Lei, "Low-frequency oscillation in electric railway depot: A comprehensive review," *IEEE Trans. Power Electron.*, vol. 36, no. 1, pp. 295–314, 2021.
[4] X. Wang and F. Blaabjerg, "Harmonic stability in power electronic-based power systems: Concept, modeling, and analysis," *IEEE Trans. Smart Grid.*, vol. 10, no. 3, pp. 2858–2870, 2019.
[5] Q. Fu, W. Du, H. Wang, and X. Xiao, "Analysis of subsynchronous oscillation caused by multiple VSCs with different dynamics under strong grid connections," *IEEE Trans. Sustain Energy.*, vol. 14, no. 4, pp. 2364–2375, 2023.
[6] R. Cvetanovic, G. Bonanno, A. Comacchio, H. Abedini, D. Biadene, and P. Mattavelli, "High frequency passivity properties of grid-connected admittance with double-sampling asymmetric dual-edge modulator," *IEEE Open J. Power Electron.*, vol. 3, pp. 856–865, 2022.
[7] X. Gao, D. Zhou, A. Anvari-Moghaddam, and F. Blaabjerg, "Stability analysis of grid-following and grid-forming converters based on state-space modelling," *IEEE Trans. Ind Appl.*, pp. 1–12, 2024.
[8] H. Gong, X. Wang, and D. Yang, "DQ-frame impedance measurement of three-phase converters using time-domain mimo parametric identification," *IEEE Trans. Power Electron.*, vol. 36, no. 2, pp. 2131–2142, 2021.
[9] E. Barocio, B. C. Pal, N. F. Thornhill, and A. R. Messina, "A dynamic mode decomposition framework for global power system oscillation analysis," *IEEE Trans. Power Syst.*, vol. 30, no. 6, pp. 2902–2912, 2015.
[10] M. Zhao, H. Yin, Y. Xue, X.-P. Zhang, and Y. Lan, "Coordinated damping control design for power system with multiple virtual synchronous generators based on Prony method," *IEEE Open Access J. Power Energy.*, vol. 8, pp. 316–328, 2021.
[11] B. McGrath, D. Holmes, and J. Galloway, "Power converter line synchronization using a discrete fourier transform (DFT) based on a variable sample rate," *IEEE Trans. Power Electron.*, vol. 20, no. 4, pp. 877–884, 2005.
[12] P. Duhamel and M. Vetterli, "Fast fourier transforms: A tutorial review and a state of the art," *Signal Process.*, vol. 19, pp. 259–299, 1990.
[13] B. Yang, K. Dai, C. Yang, H. Luo, K. He, and Z. Dai, "Improvement of recursive dft for apf with higher switching frequency to suppress wideband harmonics," *IEEE Access.*, vol. 9, pp. 144 300–144 312, 2021.
[14] H. Akagi, Y. Kanazawa, and A. Nabae, "Instantaneous reactive power compensators comprising switching devices without energy storage components," *IEEE Trans. Ind Appl.*, vol. IA-20, no. 3, pp. 625–630, 1984.
[15] M. Pradhan and M. K. Mishra, "Dual P-Q theory based energy-optimized dynamic voltage restorer for power quality improvement in a distribution system," *IEEE Trans. Ind Electron.*, vol. 66, no. 4, pp. 2946–2955, 2019.
[16] F. Harirchi and M. G. Simões, "Enhanced instantaneous power theory decomposition for power quality smart converter applications," *IEEE Trans. Power Electron.*, vol. 33, no. 11, pp. 9344–9359, 2018.
[17] V. M. Moreno, M. Liserre, A. Pigazo, and A. Dell'Aquila, "A comparative analysis of real-time algorithms for power signal decomposition in multiple synchronous reference frames," *IEEE Trans. Power Electron.*, vol. 22, no. 4, pp. 1280–1289, 2007.
[18] H. S. Lam, P. Li, B. Chen, W. M. Ng, T. Parisini, and S. Y. R. Hui, "Exponential modulation integral observer for online detection of the fundamental and harmonics in grid-connected power electronics equipment," *IEEE Trans. Control Syst Technol.*, vol. 30, no. 5, pp. 1821–1833, 2022.
[19] R. Tapia-Olvera, D. Guillen, F. Beltran-Carbajal, and L. M. Castro, "An adaptive scheme to improve prony's method performance to estimate signal parameters of power system oscillations," *IEEE Trans. Instrum Meas.*, vol. 71, pp. 1–12, 2022.
[20] H. Ye, Y. Song, Z. Zhang, and C. Wen, "Global dynamic event-triggered control for nonlinear systems with sensor and actuator faults: A matrix pencil based approach," *IEEE Trans. Automat Contr.*, vol. 69, no. 3, pp. 2007–2014, 2024.
[21] G. E. Mejia-Ruiz, R. Cárdenas-Javier, M. R. Arrieta Paternina, J. R. Rodríguez-Rodríguez, J. M. Ramirez, and A. Zamora-Mendez, "Coordinated optimal volt/var control for distribution networks via D-PMUs and EV chargers by exploiting the eigensystem realization," *IEEE Trans. Smart Grid.*, vol. 12, no. 3, pp. 2425–2438, 2021.
[22] A. Almunif, L. Fan, and Z. Miao, "A tutorial on data-driven eigenvalue identification: Prony analysis, matrix pencil, and eigensystem realization algorithm," *Int. Trans. Elect. Energy Syst.*, vol. 30, no. 4, 2020.
[23] P. J. Schmid, "Dynamic mode decomposition of numerical and experimental data," *J. Comput. Dyn.*, vol. 656, pp. 5–28, 2010.
[24] A. Alassaf and L. Fan, "Randomized dynamic mode decomposition for oscillation modal analysis," *IEEE Trans. Power Syst.*, vol. 36, no. 2, pp. 1399–1408, 2021.
[25] B. N. Kumar, S. B. Karanki, and M. S. Manikandan, "Dynamic mode decomposition based approach for accurate measurement of voltage flicker components," *IEEE Trans. Instrum Meas.*, vol. 72, pp. 1–10, 2023.
[26] C. Huang, F. Li, D. Zhou, J. Guo, Z. Pan, Y. Liu, and Y. Liu, "Data quality issues for synchrophasor applications part I: A review," *J. Mod. Power Syst. Clean Energy*, vol. 4, no. 3, pp. 342–352, 2016.
[27] N. Parmar, H. H. Refai, and T. Runolfsson, "A survey on the methods and results of data-driven koopman analysis in the visualization of dynamical systems," *IEEE Trans. Big Data.*, vol. 8, no. 3, pp. 723–738, 2022.
[28] Y. Ren, P. N. Suganthan, and N. Srikanth, "A comparative study of empirical mode decomposition-based short-term wind speed forecasting methods," *IEEE Trans. Sustain Energy.*, vol. 6, no. 1, pp. 236–244, 2015.
[29] J. Barros, R. I. Diego, and M. de Apraiz, "Applications of wavelet transform for analysis of harmonic distortion in power systems: A review," *IEEE Trans. Instrum Meas.*, vol. 61, no. 10, pp. 2604–2611, 2012.
[30] J. N. Kutz, X. Fu, and S. L. Brunton, "Multiresolution dynamic mode decomposition," *SIAM J. Appl. Dyn. Syst.*, vol. 15, no. 2, pp. 713 – 735, 2016.
[31] R. Kong, S. Sahoo, F. Blaabjerg, X. Lyu, and X. Wang, "Controller stability and low-frequency interaction analysis of railway train-network systems," *European Conf. Power Electron. Appl., EPE ECCE Europe*, pp. 1–9, 2023.
[32] G. N. Baltas, N. B. Lai, C. Sabillon, J. Cao, and P. Rodriguez, "Impedance mapping in smart grids with dynamic mode decomposition," *IEEE Energy Convers. Congr. Expo., ECCE*, pp. 1–6, 2022.
[33] E. V. Filho and P. Lopes dos Santos, "A dynamic mode decomposition approach with hankel blocks to forecast multi-channel temporal series," *IEEE Control Syst Lett.*, vol. 3, no. 3, pp. 739–744, 2019.
[34] M. E. Torres, M. A. Colominas, G. Schlotthauer, and P. Flandrin, "A complete ensemble empirical mode decomposition with adaptive noise," *ICASSP IEEE Int Conf. Acoust Speech Signal Process.*, pp. 4144–4147, 2011.
[35] Y. Zhou, H. Hu, X. Yang, J. Yang, Z. He, and S. Gao, "Low frequency oscillation traceability and suppression in railway electrification systems," *IEEE Trans. Ind Appl.*, vol. 55, no. 6, pp. 7699–7711, 2019.
[36] H. Hu, Y. Zhou, J. Yang, Z. He, and S. Gao, "A practical approach to mitigate low-frequency oscillation in railway electrification systems," *IEEE Trans. Power Electron.*, vol. 33, no. 10, pp. 8198–8203, 2018.
[37] Z. Zou, G. Buticchi, and M. Liserre, "Analysis and stabilization of a smart transformer-fed grid," *IEEE Trans. Ind Electron.*, vol. 65, no. 2, pp. 1325–1335, 2018.
[38] Z. Yang, C. Shah, T. Chen, J. Teichrib, and R. W. De Doncker, "Virtual damping control design of three-phase grid-tied PV inverters for passivity enhancement," *IEEE Trans. Power Electron.*, vol. 36, no. 6, pp. 6251–6264, 2021.
[39] Y. Liao, X. Wang, and F. Blaabjerg, "Passivity-based analysis and design of linear voltage controllers for voltage-source converters," *IEEE Open J. Ind. Electron. Soc.*, vol. 1, pp. 114–126, 2020.
[40] H. Tao, W. Lu, H. Hu, X. Zhu, and Z. He, "Stability enhancement method based on adaptive virtual impedance control for a PV-integrated electrified railway system," *IEEE Trans. Veh. Technol.*, pp. 1–12, 2024.
[41] R. Kong, S. Sahoo, X. Lyu, X. Wang, and F. Blaabjerg, "Quantitative assessment mechanism of low frequency oscillations in train-network systems," *Sustainable Energy, Grids and Networks*, vol. 39, p. 101410, 2024.

Rui Kong (S'23) received the B.Sc. and M.Eng. degrees in Electrical Engineering from Southwest Jiaotong University, Chengdu, China, in 2019 and 2022, respectively. He is currently working toward a Ph.D. degree in the Department of Energy, Aalborg University (AAU Energy), Aalborg, Denmark.

His research interests include the data-driven identification and control, modeling, and stability analysis of power electronic converter-based systems.

Subham Sahoo (S'16–M'18–SM'23) received the B.Tech. & Ph.D. degree in Electrical and Electronics Engineering from VSSUT, Burla, India and Electrical Engineering at Indian Institute of Technology, Delhi, New Delhi, India in 2014 & 2018, respectively. He is currently an Assistant Professor in the Department of Energy, Aalborg University (AAU), Denmark, where he is also the vice-leader of the research group on Reliability of Power Electronic Converters (ReliaPEC) in AAU Energy.

He is a recipient of the Indian National Academy of Engineering (INAE) Innovative Students Project Award for the best PhD thesis in 2019. He is also selected into EU-US National Academy of Engineering (NAE) Frontier of Engineering (FOE) Class of 2021. He is an affiliate of the Danish Data Science Academy (DDSA), European Lab for Learning & Intelligent Systems (ELLIS) and Lundbeck Foundation Investigator Network. He was also a distinguished reviewer for IEEE Transactions on Smart Grid in 2020. He is currently the vice-chair of IEEE PELS Technical Committee (TC) 10 on Design Methodologies. He is an Associate Editor on IEEE Transactions on Transportation Electrification.

His research interests are control, optimization, cybersecurity and stability of power electronic dominated grids, application of artificial intelligence and machine learning in power electronic systems.

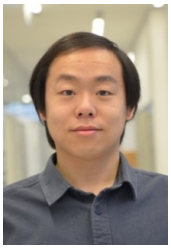

Yubo Song (S'18–M'24) received the B.Sc. and M.Eng. degrees in Electrical Engineering from Shanghai Jiao Tong University, Shanghai, China, in 2016 and 2019, and Ph.D. degree in Energy Technology from Aalborg University, Aalborg, Denmark, in 2023, respectively. He is currently a Postdoc in the Department of Energy, Aalborg University, Aalborg, Denmark.

From May to July 2022, he was a visiting researcher with the ELITE Grid Research Lab, University of Alberta, Edmonton, AB, Canada. He is a recipient of the Spin-Outs Denmark grant in 2024.

His research interests include the control, stability and reliability of power electronic systems and power electronic dominated grids.

Yi Xiao (S'22) received the B.S. degree in Electrical Engineering from Southwest Jiaotong University, Chengdu, China, in 2022. He is currently working toward the Ph.D. degree in power electronics with Zhejiang University, Hangzhou, China.

His research interests include modeling, stability, and control of grid-forming converters and power-electronic-based power systems.

Chao Gao received the B.S. degree from Wuhan University, Wuhan, China, in 2018, and the M.S. degree from Huazhong University of Science and Technology, Wuhan, China, in 2021, both in electrical engineering. He is currently working toward the Ph.D. degree from the Chinese University of Hong Kong, Hong Kong. He is guest Ph.D. Student with the Department of Energy, Aalborg University, Aalborg, Denmark since 2023.

His research interests include modeling and control of power electronic converters.

Frede Blaabjerg (S'86–M'88–SM'97–F'03) received the Ph.D. degree in electrical engineering from Aalborg University, Aalborg, Denmark, in 1995.

He was with ABB-Scandia, Randers, Denmark, from 1987 to 1988. He became an Assistant Professor in 1992, an Associate Professor in 1996, and a Full Professor of power electronics and drives in 1998. From 2017 he became a Villum Investigator. He is honoris causa at University Politehnica Timisoara (UPT), Romania, and Tallinn Technical University (TTU) in Estonia. His current research interests include power electronics and its applications, such as in wind turbines, PV systems, reliability, harmonics, and adjustable speed drives. He has published more than 600 journal papers in the fields of power electronics and its applications. He is the co-author of four monographs and editor of ten books in power electronics and its applications.

He has received 32 IEEE Prize Paper Awards, the IEEE PELS Distinguished Service Award in 2009, the EPE-PEMC Council Award in 2010, the IEEE William E. Newell Power Electronics Award 2014, the Villum Kann Rasmussen Research Award 2014, the Global Energy uPrize in 2019 and the 2020 IEEE Edison Medal. He was the Editor-in-Chief of the IEEE TRANSACTIONS ON POWER ELECTRONICS from 2006 to 2012. He has been a Distinguished Lecturer for the IEEE Power Electronics Society from 2005 to 2007 and for the IEEE Industry Applications Society from 2010 to 2011 as well as 2017 to 2018. In 2019-2020 he served as President of the IEEE Power Electronics Society. He is Vice-President of the Danish Academy of Technical Sciences too. He is nominated in 2014-2019 by Thomson Reuters to be between the most 250 cited researchers in Engineering in the world.